Journal of Photochemistry and Photobiology A: Chemistry 211 (2010) 185–192

Contents lists available at ScienceDirect

Journal of Photochemistry and Photobiology A: Chemistry

journal homepage: www.elsevier.com/locate/jphotochem

Photocatalytic degradation of organic molecules in water: Photoactivity and reaction paths in relation to TiO_2 particles features

Cecilia Bernardini, Giuseppe Cappelletti, Maria Vittoria Dozzi, Elena Selli*

Dipartimento di Chimica Fisica ed Elettrochimica, Università degli Studi di Milano, Via Golgi 19, I-20133 Milano, Italy

ARTICLE INFO

Article history:
Received 11 January 2010
Received in revised form 19 February 2010
Accepted 15 March 2010
Available online 20 March 2010

Keywords:
TiO_2 photocatalysts
Photodegradation
Azo dye
Formic acid
H_2O_2 photoproduction
Ti^{3+} in TiO_2

ABSTRACT

Anatase–rutile and anatase–brookite–rutile composite nanocrystals were synthesized by a controlled sol–gel reaction followed by hydrothermal growth and by mechanically mixing pure crystalline phase precursors, respectively. Their physicochemical and photocatalytic properties were investigated in comparison with those of several home-made and commercial pure anatase, rutile and mixed phase TiO_2 samples. In particular, the phase composition and the crystallite size were determined by X-ray diffraction measurements. The photocatalytic degradation of the azo dye Acid Red 1 (AR1) and of formic acid (FA) in aqueous suspension were employed as test reactions. Hydrogen peroxide evolution, the main reductive process occurring in parallel, was also monitored during the runs. The investigated photocatalysts exhibit different photoactivity scales towards the two organic substrates, depending on the prevailing photodegradation path. High surface area anatase samples were particularly active in FA degradation, principally occurring through direct interaction with photoproduced valence band holes, whereas rutile samples, even possessing high surface areas, but exhibiting poor wettability, were scarcely active. A good linear correlation was found between H_2O_2 evolution and the rate of AR1 photodegradation on the investigated series of photocatalysts, whereas no H_2O_2 was detected during FA mineralization, apart in the case of a low surface area anatase sample, whose peculiar photocatalytic properties were ascribed to the presence of Ti^{3+} ions in its structure.

1. Introduction

In recent years great efforts have been devoted to the study of the photocatalytic degradation of organic and inorganic contaminants of water and air [1–4]. The overall efficiency of photocatalytic processes depends, first of all, on several physicochemical features of the semiconductor, such as the position of its band gap potential, the crystalline phase composition, the surface properties, the mobility and recombination rate of the charge carriers generated during UV-light irradiation. Also the chemical and adsorption properties of the substrates, as well as the adopted experimental conditions (pH, substrate concentration, photocatalyst amount and form), play important roles.

Titanium dioxide is the most widely used photocatalyst, because it provides the best compromise between photocatalytic performance and stability in most chemical environments. In nature, TiO_2 can crystallize in the three polymorphs anatase, rutile and brookite. Anatase is thermodynamically less stable than rutile and exhibits a shorter wavelength absorption edge. Frequently present in nanosized TiO_2 particles, it is largely recognized to be the most active phase in oxidative detoxification reactions. Mixtures of the abovementioned polymorphs of TiO_2 may produce intriguing effects on charge carrier transfer processes in photocatalytic applications [5–10].

The possible relation between the physicochemical features of TiO_2 (type of crystalline phase, surface area and hydrophilicity, crystallite dimensions) and its photocatalytic activity in the degradation of two organic substrates has been investigated in the present work. A wide series of pure and mixed phases TiO_2 photocatalysts has been examined, including both commercial and home-synthesized samples with tailored properties, expressly prepared according to different procedures, including sol–gel synthesis followed by hydrothermal growth and mixing of pure crystalline phases followed by calcination.

The azo dye Acid Red 1 (AR1, see Scheme 1), whose photocatalytic degradation, occurring through an oxidative, mainly •OH radicals-mediated path, has been widely investigated by us [11–16], was chosen as model pollutant to be photodegraded. Also formic acid (FA) was studied as degradation substrate, mainly because it undergoes direct photocatalytic oxidation to CO_2 and H_2O without forming any stable intermediate. This allows a more straightforward interpretation of the kinetic results. The evolution of hydrogen peroxide, generated by the combination of O_2 with conduction band electrons, was also monitored during all

* Corresponding author. Tel.: +39 02 50314237; fax: +39 02 50314300.
E-mail address: elena.selli@unimi.it (E. Selli).

1010-6030/$ – see front matter © 2010 Elsevier B.V. All rights reserved.
doi:10.1016/j.jphotochem.2010.03.006

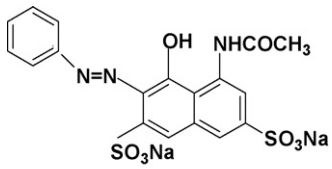

Acid Red 1 (AR1)

Scheme 1.

photodegradation runs, to get information on the main reductive process occurring in parallel to the oxidation of the two organic substrates.

2. Experimental

2.1. Materials

Most chemicals, *i.e.* Acid Red 1 (AR1) and formic acid (FA), purity 95–97%, were purchased from Aldrich. Peroxidase (type II, from horseradish) was a Sigma product. Tris(hydroxymethyl)–aminomethane (TRIS), 99.7%, was purchased from Baker Chemicals and *p*-hydroxyphenylacetic acid (POHPA), >98%, was purchased from Fluka. They were all employed as received, apart from AR1, which was purified by crystallization from methanol, as already described [11]. Water purified by a Milli-Q apparatus (Millipore) was used to prepare solutions and suspensions.

Apart from the well-known commercial P25 Degussa (anatase–rutile composite), all of the investigated TiO_2 samples were labeled with capital letters indicating polymorphs, A standing for anatase, R for rutile and B for brookite, and with ensuing numbers indicating their surface area, expressed in $m^2\,g^{-1}$. Home-made photocatalysts, comprising pure rutile, mixed anatase–rutile and ternary mixed anatase–brookite–rutile samples, were compared with commercial pure phase anatase A284, A136, A9 (Alfa Aesar), pure phase rutile R3 (Aldrich) and the two anatase–rutile mixed phase samples P25 (Degussa) and AR43 (Alfa Aesar). The complete series of photocatalysts investigated in the present study is displayed in Table 1.

The synthesis of pure rutile photocatalysts R192 and R130 was reported previously [17]. Briefly, a $TiCl_3$ solution (12% in hydrochloric acid) was neutralized by NH_3 addition, in order to achieve pH 4. The mixture was kept stirred under O_2 stream ($10\,L\,h^{-1}$), up to the disappearance of the blue color. The final slurry was centrifuged and the wet precursor (R) was dried in oven at 80 °C overnight and then calcined under an oxygen stream, at 200 °C (R192 sample) or at 300 °C (R130 sample), respectively.

The mixed anatase–rutile AR173, AR144 and AR130 photocatalysts were prepared by mechanical mixing of different amounts of commercial A284 with pure rutile precursor (R), followed by calcination at 300 °C. The A284 to R precursor initial ratios were 90:10 for AR172, 80:20 for AR144 and 70:30 for AR130.

Ternary mixed anatase–brookite–rutile samples were prepared according to two different sol–gel procedures. ABR172 was obtained by 500 h—long hydrothermal growth in water at spontaneous pH and 50 °C of an amorphous sol–gel precursor in the presence of seeds of both an anatase–brookite sample, prepared in a previous work (sample T_hydro in Ref. [13]), and rutile R130. 0.1 g of each crystalline sample were mixed with 3.0 g of amorphous precursor; the so obtained final product was not calcined. Mixed anatase–brookite–rutile ABR155 was obtained by mechanical mixing the precursor of the above-mentioned T_hydro anatase-brookite sample [18] with the rutile (R) precursor (85/15 weight ratio), followed by calcination at 300 °C.

2.2. Photocatalysts characterization

UV–vis diffuse reflectance (DR) spectra of TiO_2 samples were recorded using a Lambda 19, PerkinElmer spectrophotometer equipped with an RSA-PE-20 integrating sphere assembly, using a calibrated SRS-99-010 Spectralon Reflectance Standard, produced by Labsphere, as reference material.

Room temperature X-ray powder diffraction (XRPD) patterns were collected between 10° and 80° (2θ range, $\Delta 2\theta = 0.02°$) with a Siemens D500 diffractometer, using Cu Kα radiation. Rietveld refinement was performed using the GSAS software suite and its graphical interface EXPGUI [19]. The average diameter of the crystallites, $\langle d \rangle$, was estimated from the most intense reflection of the TiO_2 anatase (1 0 1) and rutile (1 1 0) phases, using the Scherrer equation [17].

Scanning electron microscopy (SEM) photographs were acquired by LEO 1430. Specific surface areas were determined by the classical BET procedure using a Coulter SA 3100 apparatus. The "calculated" diameter of the particles, d_{BET}, was obtained by means of the following formula, under the assumption that the particles are composed of single crystals with spherical geometry and have negligible porosity and surface roughness:

$$d_{BET}\ (\text{Å}) = \frac{6 \times 10^4}{S_{BET} \times \rho}$$

ρ = average titanium dioxide density ($4.0\,g\,cm^{-3}$).

EPR spectra were recorded at room temperature by means of an ESP-300 Bruker EPR spectrometer, operating in the X-band.

Table 1
BET surface area, quantitative phase composition from XRD analysis, mean diameter $\langle d_A{}^{101} \rangle$ of anatase and $\langle d_R{}^{110} \rangle$ of rutile crystallites, calculated from XRD patterns employing the Scherrer equation, and mean crystallite diameter d_{BET}, according to BET measurements.

Photocatalyst	Supplier	S_{BET} ($m^2\,g^{-1}$)	%Anatase	%Rutile	%Brookite	$\langle d_A{}^{101} \rangle$ (nm)	$\langle d_R{}^{110} \rangle$ (nm)	d_{BET} (nm)
A284	Alfa Aesar	284	100	–	–	9 ± 1	–	5
A136	Alfa Aesar	136	100	–	–	18 ± 3	–	11
A9	Alfa Aesar	9	100	–	–	86 ± 18	–	167
R192	Home-made	192	–	100	–	–	6 ± 1	8
R130	Home-made	130	–	100	–	–	7 ± 1	11
R3	Aldrich	3	–	100	–	–	93 ± 20	500
AR173	Home-made	173	95	5	–	12 ± 2	–	9
AR144	Home-made	144	86	14	–	15 ± 2	17 ± 3	10
AR130	Home-made	130	80	20	–	17 ± 3	20 ± 3	11
P25	Degussa	48	78	22	–	25 ± 5	35 ± 8	31
AR43	Alfa Aesar	43	91	9	–	35 ± 8	–	35
ABR172	Home-made	172	51	9	40	7 ± 1	9 ± 1	9
ABR155	Home-made	155	42	27	31	7 ± 1	8 ± 1	10

2.3. Photocatalytic activity determination

All kinetic runs were performed at 30 ± 1 °C, under atmospheric conditions, in a magnetically stirred, 600 mL-cylindrical Pyrex reactor, employing an experimental setup similar to that already described [12,20]. Irradiation was performed by means of a 250 W iron halogenide lamp (Jelosil, model HG 200), emitting in the 315–400 nm wavelength range, with a mean emission intensity on the reactor of 3.0×10^{-7} Einstein s^{-1} cm^{-2}, as periodically checked by ferrioxalate actinometry [21].

All photocatalytic runs were performed in aqueous suspensions containing a fixed amount of TiO_2, *i.e.* 0.1 g L^{-1}. The initial concentration of organic substrate was 2.5×10^{-5} M for AR1 and either 0.5 or 1.0×10^{-3} M for FA. Suspensions containing 0.2 g L^{-1} of TiO_2 were preliminarily sonicated for 30 min in the reactor by means of a Heat Systems Ultrasonics, model W-385, apparatus, emitting at 20 kHz. Then the appropriate volume of aqueous solution containing the organic substrate was added up to the desired final volume and concentration. The so formed suspension was magnetically stirred in the dark at 30 °C for about 30 min, to attain the adsorption–desorption equilibrium of the substrate on the photocatalyst surface, before starting irradiation. All kinetic runs were followed up to a degradation yield of at least 70%. 4 mL-samples were periodically withdrawn from the reactor and analyzed for residual substrate content, after removal of the TiO_2 particles by centrifugation at 4000 rpm for 20 min, by means of a EBA-20 Hettich centrifuge.

The cleavage of the AR1 azo bond, consequent to •OH radicals attack and leading to bleaching in the visible region [22], was monitored by spectrophotometric analysis at 531 nm [11], by means of a PerkinElmer Lambda 16 spectrophotometer. FA concentration was monitored using a total organic carbon (TOC) analyzer (Shimadzu Instruments, TOC-5000A) in the total carbon (TC) and inorganic carbon (IC) modes [13]. FA concentration was evaluated as total organic carbon concentration, calculated as the difference between TC and IC analyses.

All kinetic runs were repeated at least twice, to test their reproducibility. They were performed under natural pH conditions, to avoid the addition of species which might interfere with the photoinduced electron transfer processes occurring at the solid–liquid interface. The pH of the suspensions was always measured at the beginning and at the end of the runs by means of an Amel, model 2335, pH meter. During AR1 photocatalytic degradation, the pH decreased from an initial value in the 6.2–5.5 range, depending on the photocatalyst, to a final value in the 4.5–3.8 range, as a consequence of the production of stable acids, due to the removal of the sulfonic groups of AR1 and the oxidation of the azo double bond [22]. By contrast, a pH increase occurred during FA degradation, from initial values around 3.7 to *ca.* 4.8, as a consequence of FA mineralization to CO_2 and H_2O.

Hydrogen peroxide concentration was monitored during the photodegradation runs by fluorimetric analysis (λ_{ex} = 316.5 nm, λ_{em} = 408.5 nm) of the fluorescent dimer formed in the horseradish peroxidase-catalyzed reaction of hydrogen peroxide with POHPA, using a 605-10S PerkinElmer fluorescence spectrophotometer, as already described [11,13]. Measurements were performed by adding 0.5 mL of a solution containing peroxidase to a 2 mL volume of surnatant after centrifugation. The peroxidase solution was prepared by dissolving 8 mg of POHPA and 2 mg of peroxidase in 50 mL of a buffer solution at pH 8.8, obtained by adding a few drops of HCl to a 0.1 M TRIS solution. Test tubes were maintained in the dark for *ca.* 30 min before recording the fluorescence signal.

AR1 adsorption measurements were performed in aqueous suspensions containing 1.0 g L^{-1} of TiO_2 and an overall AR1 concentration of 2.5×10^{-5} M in AR1. The suspensions were magnetically stirred for 24 h in the dark. Samples were withdrawn after different times, centrifuged and spectrophotometrically analyzed for AR1 determination in the surnatant. The adsorption data after 6 h—long equilibration were considered as most reliable. The fraction of FA adsorbed on TiO_2 was always almost negligible, even in the presence of a tenfold higher amount of TiO_2 with respect to that employed during the runs: the very small FA concentration variations in the aqueous phase could not be determined with enough accuracy [13].

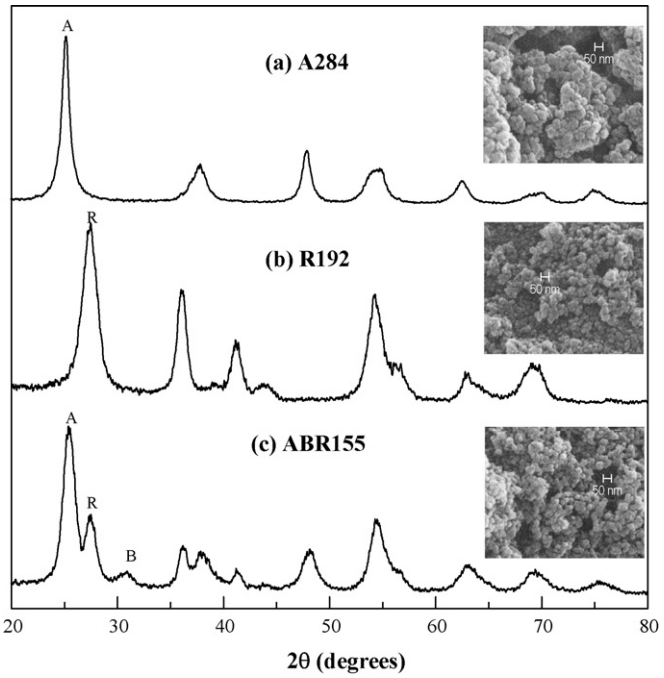

Fig. 1. Powder X-ray diffraction lines of (a) A284 (pure anatase), (b) R192 (pure rutile) and (c) ABR155 (ternary) samples. Insets: corresponding SEM images.

3. Results and discussion

3.1. Photocatalysts characterization

X-ray diffraction lines of selected samples are shown in Fig. 1, whereas Table 1 reports, for all photocatalysts, the surface area, the phase composition and the average crystallite sizes, as obtained from the analysis of X-ray profiles, $\langle d_A{}^{101} \rangle$ and $\langle d_R{}^{110} \rangle$, and from specific surface area measurements, d_{BET}.

Fig. 1a shows that only the diffraction lines of the anatase phase are appreciable in the case of sample A284. By elaboration of the 101, most intense, XRD peak, a crystallites size of 9 nm can be obtained. The surface area is consistently rather large (Table 1). The SEM micrograph of this sample (inset of Fig. 1a) shows the presence of aggregates of variable sizes (30–100 nm). The d_{BET} value of A284 reported in Table 1 might be underestimated because of its relatively high porosity in the low-pore-size regime and possibly also because of surface roughness. The structural and morphological data of the two pure anatase commercial samples A136 and A9, also reported in Table 1, evidence progressively larger crystallite sizes with decreasing surface areas. In the case of A9, a comparison between $\langle d_A{}^{101} \rangle$ and d_{BET} values is indicative of a large degree of aggregation/sintering between crystallites.

Fig. 1b shows the diffraction lines of home-made pure rutile R192: only the lines pertaining to the rutile structure can be appreciated. The crystallite size is 6 nm, more than one order of magnitude smaller than the crystallite size of high purity commercial rutile R3, leading to an ensuing much larger surface area (Table 1, third column). The SEM micrograph of R192, also reported

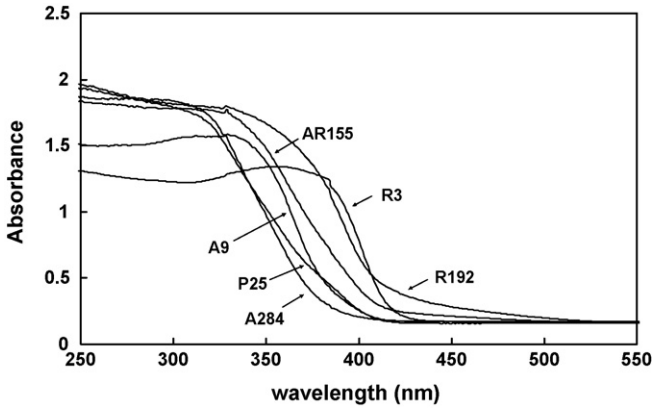

Fig. 2. Absorption spectra of selected TiO_2 samples (see Table 1).

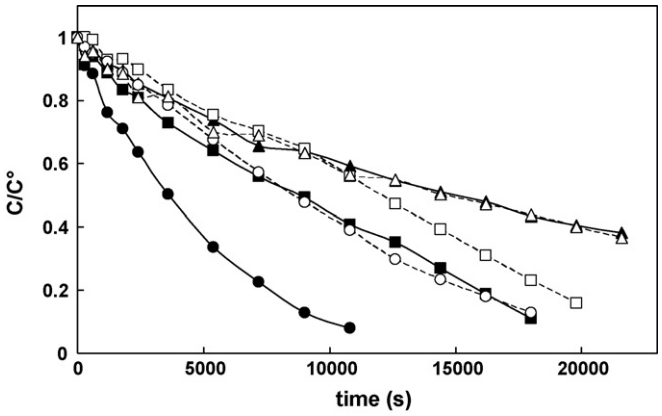

Fig. 3. AR1 concentration profiles during photocatalytic runs in the presence of 0.1 g L^{-1} of A9 (circles), A136 (squares) and R3 (triangles). Full symbols and continuous lines refer to suspensions pre-sonicated for 30 min, open symbols and dashed lines refer to untreated suspensions.

in the inset of Fig. 1b, exhibits smaller and looser aggregates composed by well defined particles. The excellent agreement between $\langle d_R{}^{110}\rangle$ and d_{BET} values (Table 1) indicates that the particles are actually present mainly as single crystals with negligible aggregation or sintering between the crystallites.

Fig. 1c shows the XRD spectrum of mixed phase ABR155 sample, chosen to exemplify the co-presence of the three TiO_2 polymorphs. Small crystallite sizes (<10 nm) can be envisaged (see inset of Fig. 1c), having similar dimensions among the three phases, fully compatible with the d_{BET} value (Table 1). Further structural data of anatase–rutile mixed samples are collected in Table 1. In general, from the inspection of the structural features reported in this table one may observe that home-made TiO_2 samples consistently show larger surface areas and smaller crystallite sizes than commercial ones.

The UV–vis DR spectra of selected TiO_2 samples are shown in Fig. 2. In general, all pure anatase samples exhibit a very similar absorption behavior, with an absorption edge around 380 nm, as exemplified by the absorption spectrum of A284 reported in Fig. 2. The only exception is A9, whose absorption pattern is markedly shifted towards longer wavelengths. Mixed phase home-made samples, *e.g.* AR155 in Fig. 2, exhibit a red-shifted band gap absorption, almost half way between the absorption edge of pure anatase and that of pure rutile, whose absorption extends towards the visible region, up to *ca.* 420 nm, because of its reduced band gap with respect to pure anatase. The absorption spectra of mixed phase commercial AR43 (not shown) and P25 samples are very similar, both being shifted to shorter wavelength with respect to mixed phase home-made samples and both exhibiting a perceptible change in the absorption *vs.* wavelength slope in the 380–400 nm range.

3.2. Photocatalytic activity

3.2.1. AR1 photocatalytic degradation

Preliminary AR1 adsorption measurements were carried out in the dark, employing a 10 times higher amount of commercial TiO_2 photocatalysts with respect to the amount employed in kinetic runs. AR1 adsorption never exceeded 10% of the initial AR1 concentration, pointing to a limited AR1 adsorption on TiO_2 at the beginning of the runs, under pH conditions very close to the point of zero charge of TiO_2 [23]. Thus, AR1 concentration in the aqueous phase practically coincided with the overall AR1 content of the suspensions.

AR1 was perfectly stable in aqueous solution under the here adopted irradiation conditions [11], whereas its concentration decreased, always according to a first order rate law, during the photocatalytic runs in aqueous suspensions containing the investigated TiO_2 photocatalysts. Examples of AR1 concentration *vs.* irradiation time curves are shown in Fig. 3.

Pre-sonication, favoring the dispersion of the photocatalysts particles in the aqueous suspensions, was found to influence the photocatalytic reaction rate to a variable extent, depending on the photocatalyst. The maximum AR1 degradation rate increase was verified for A9, with an almost doubled reaction rate upon ultrasound pre-treatment of the aqueous suspension (see Fig. 3), whereas this treatment induced less remarkable activation of high surface area pure anatase A284 and A136 samples. This is in line with the $\langle d_A{}^{101}\rangle$ value lower than the d_{BET} value reported for A9 in Table 1, indicating significant crystallites aggregation. By contrast, the photocatalytic activity of commercial R3 and A43 proved to be totally insensitive to preliminary sonication, a fact already ascertained also for P25 [20]. This is not surprising for AR43 and P25, their average crystallite sizes practically coinciding with their d_{BET} values (Table 1), whereas it is unexpected for R3, having d_{BET} greater than $\langle d_R{}^{110}\rangle$.

Based on these results, all aqueous suspensions containing the photocatalysts were treated with ultrasound for a standard time prior to the addition of the organic substrates, in order to ensure de-aggregation of the photocatalyst particles and maximization of their surface area in contact with the aqueous phase.

The first order rate constants of AR1 photocatalytic degradation in the presence of all photocatalysts investigated in the present study are collected in Fig. 4. No direct correlation between the reaction rate and the photocatalysts surface area or phase composition

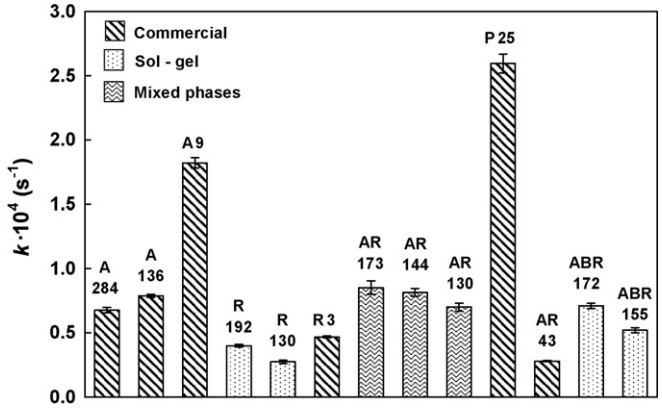

Fig. 4. First order rate constants of AR1 photocatalytic degradation in the presence of 0.1 g L^{-1} of TiO_2 photocatalysts (see Table 1).

can be envisaged. The most efficient photocatalyst was P25, characterized by a relatively low surface area and a binary anatase–rutile crystalline phase composition, surprisingly followed by A9, a low surface area pure anatase. The other commercial, higher surface area pure anatase photocatalysts proved to be less efficient, exhibiting similar photocatalytic activity, not correlated to their surface area. Furthermore, A43 showed remarkably poorly active, in spite of its phase composition, surface area and absorption properties similar to those of P25.

Also home-made mixed phase photocatalysts AR173, AR144 and AR130 exhibit a photocatalytic activity lower than that of P25, but very similar to that of pure anatase A136 and slightly increasing with their surface area. These three mixed anatase–rutile samples were prepared starting from different percent amounts of rutile seeds, but finally had quite similar crystalline phase composition (Table 1), due to partial polymorph transformation during calcination.

Finally, the presence of brookite in sol–gel synthesized, mixed anatase, rutile and brookite phase materials ABR155 and ABR172 did not impart any synergistic increase of photoactivity, which thus appears mostly related to their anatase content. The higher photoactivity of ABR172 compared to ABR155 may be consequent to its higher surface area and/or different phase composition, in particular its higher anatase content (51% *vs.* 42%), or higher amount of surface hydroxyl groups (ABR172 did not undergo any calcination step).

In general, the phase composition may affect not only the intrinsic photoactivity, but also the wettability of the photocatalyst powders in water [24], which has a paramount importance in guaranteeing effective particles dispersion in the aqueous phase and efficient light absorption by the semiconductor, originating charge separation and inter-phase electron transfer processes. Indeed, all our pure rutile samples showed low photoactivity (Fig. 4), although their absorption spectrum extends to the visible region (Fig. 2) and the home-made ones possess outstanding surface area and very small crystallite dimensions (Table 1). Because of their poor wettability in water, we visually observed that they tended to adhere to the reactor walls and to aggregate at the air–water inter-phase during the runs. Consequently, the extent of their surface area, and also the ultrasound pre-treatment to increase their dispersion in water (Fig. 3), had scarce influence on their photoactivity, which thus resulted severely limited by their lack of wettability. Of course, other intrinsic characteristics of rutile, such as its low conduction band edge preventing electron transfer to O_2, can also be invoked as the origin of its low photoactivity.

3.2.2. H_2O_2 evolution during AR1 photocatalytic degradation

The evolution of hydrogen peroxide was monitored during the runs to ascertain how the rate of AR1 oxidative degradation correlates to the main parallel reductive path occurring under irradiation. H_2O_2 is generated *via* reduction of molecular oxygen adsorbed on the photocatalyst surface by the electrons photo-promoted into the TiO_2 conduction band, e_{CB}^-, according to reactions (1) and (2) [25]:

$$O_2 + e_{CB}^- \rightarrow O_2^{\bullet -} \quad (1)$$

$$O_2^{\bullet -} + e_{CB}^- + 2H^+ \rightarrow H_2O_2 \quad (2)$$

The so formed hydrogen peroxide may undergo photoinduced degradation mainly on the photocatalyst surface, by direct reaction with photogenerated charged species, *i.e.* valence band holes, h_{VB}^+, and conduction band electrons, e_{CB}^-, and/or other reactive species, such as hydroxyl radicals and the superoxide radical anion [26–28]. Thus, hydrogen peroxide could be detected in photocatalytic reaction systems only if its formation rate is greater than its consumption rate under irradiation [13].

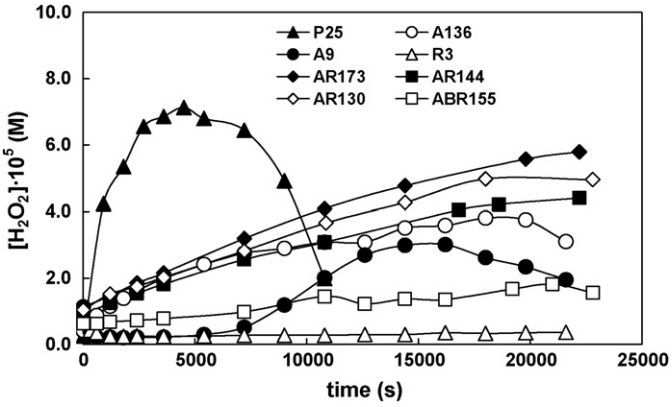

Fig. 5. H_2O_2 evolution during AR1 photocatalytic degradation on selected TiO_2 photocatalysts (see Table 1).

The H_2O_2 concentration profiles determined during the photocatalytic degradation of AR1 in the presence of most of the investigated photocatalysts are shown in Fig. 5. The highest levels of hydrogen peroxide were attained in the presence of P25: in this case H_2O_2 concentration rapidly increased during AR1 photodegradation, reached a maximum value for a *ca.* 80–90% AR1 photodegradation yield and then decreased, when the suspension was completely bleached. An almost identical H_2O_2 concentration profile was observed during the photocatalytic degradation of benzoic acid in the presence of P25 [13].

By contrast, hydrogen peroxide evolved in a much more gradual way during AR1 photodegradation on the other photocatalysts (Fig. 5). Relatively high quantities of hydrogen peroxide were continuously generated on mixed phase AR173, AR144 and AR130, though at a continuously decreasing rate, up to complete AR1 degradation. Progressively lower H_2O_2 amounts accumulated, in the order, on pure anatase A136 and A284 (not shown) and mixed phases ABR172 (not shown) and ABR155 samples, with H_2O_2 concentration profiles usually starting to decline after complete AR1 degradation. This behavior most probably reflects the relatively lower photocatalytic activities of these samples, leading to lower AR1 degradation and H_2O_2 production rates on their surface. Sol–gel synthesized and mixed phases samples evolved lower amounts of hydrogen peroxide, the lower was their anatase content, down to pure rutile samples, which exhibit almost no H_2O_2 evolution during AR1 photocatalytic degradation (Fig. 5).

In general, the higher was the AR1 decomposition rate, the higher was the accumulated H_2O_2 amount. Fig. 6 shows that a linear

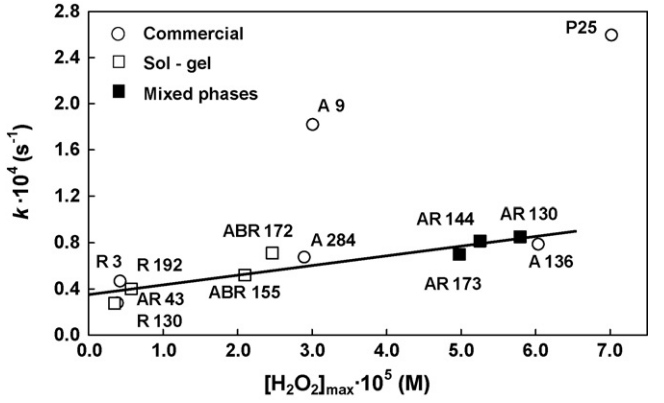

Fig. 6. Correlation between first order rate constants of AR1 photodegradation on different TiO_2 photocatalysts and maximum H_2O_2 concentration attained during the photodegradation runs.

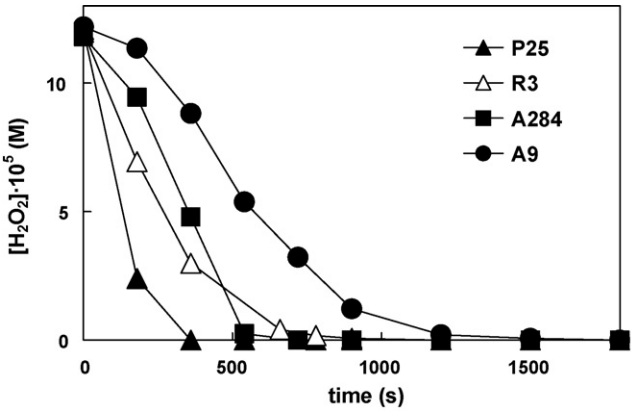

Fig. 7. Hydrogen peroxide concentration profiles in irradiated aqueous suspensions containing 0.1 g L^{-1} of photocatalyst and no organic substrate.

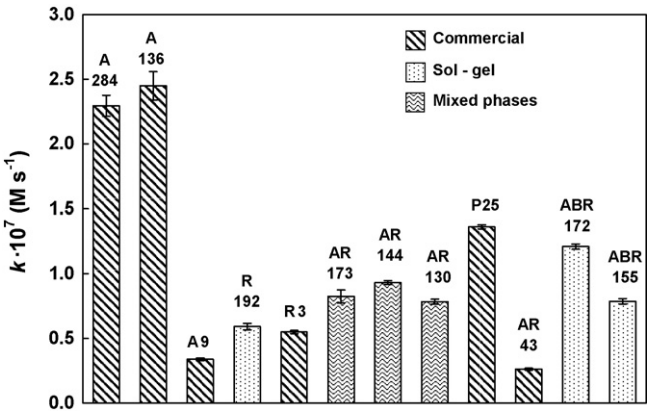

Fig. 8. Zero-order rate constants of FA photocatalytic degradation in the presence of 0.1 g L^{-1} of TiO_2 photocatalysts (see Table 1).

correlation exists between the rate constants of AR1 photodegradation and the maximum H_2O_2 concentration values attained during the photocatalytic runs. This is consistent with H_2O_2 production through a reductive path [reactions (1) and (2)] simultaneous to the photocatalytic oxidation of the organic substrate. If O_2 molecules adsorbed on the photocatalyst surface are able to efficiently act as scavengers of photoexcited conduction band electrons according to reaction (1), photogenerated valence band holes become more easily available for oxidation reactions.

Fig. 6 also evidences that only P25 and A9 markedly deviated from the behavior common to all other photocatalysts, the maximum H_2O_2 concentration values attained during the photocatalytic runs in their presence being lower than expected in relation to the measured AR1 photodegradation rate constants.

The H_2O_2 concentration profile during AR1 photodegradation in the presence of A9 is very peculiar (Fig. 5), exhibiting an induction period up to a AR1 degradation yield close to 90%, during which no H_2O_2 could be detected, followed by relatively fast hydrogen peroxide accumulation and subsequent decline. Thus, in this case the photocatalytic degradation of AR1 appears to be in competition with molecular oxygen reduction by conduction band electrons, leading to H_2O_2 formation. According to previous cyclic voltammetry measurements [12], the reduction potential of AR1 is −0.33 V (NHE), *i.e.* slightly lower than the conduction band edge of TiO_2 (E°_{CB} (V) = −0.13 to −0.059 pH *vs.* NHE). Consequently, electron transfer from the TiO_2 conduction band to AR1 would in principle be allowed, inducing the reduction of the diazo moiety of AR1, followed by its cleavage and consequent overall bleaching [29].

In order to have a better insight into the balance between the H_2O_2 photocatalytic formation and degradation rates, determining the amount of H_2O_2 accumulated during AR1 photocatalytic degradation runs, the degradation of hydrogen peroxide, either in the absence and in the presence of the investigated photocatalysts, was monitored under irradiation conditions identical to those employed in AR1 photocatalytic degradation, starting from a H_2O_2 concentration similar to that attained during the runs. H_2O_2 was found to be perfectly photostable in aqueous solution [13] and to decompose only in the presence of TiO_2 particles. The selected results shown in Fig. 7 confirm that P25 is very photoactive: on its surface H_2O_2 is produced at relatively high rate and also photodegraded at relatively high rate. The various anatase, rutile and mixed phase samples were generally similarly active in H_2O_2 photodegradation. Thus, the lack of H_2O_2 accumulation during AR1 degradation runs on rutile samples (Fig. 5) is simply a consequence of low production rate and relatively faster degradation on their surface. Finally, the relatively slow H_2O_2 degradation on A9 (Fig. 7) seems to exclude that the initial induction period observed in the H_2O_2 profile during AR1 photocatalytic degradation (Fig. 5) could be attributed to fast degradation on its surface and points to a very low H_2O_2 formation rate in the initial steps of AR1 photodegradation.

The outstanding photocatalytic activity of P25, which is manufactured by flame hydrolysis of titanium tetrachloride at high temperature, has been convincingly attributed to its peculiar structure consisting of bulk material having a nanostructured arrangement of interwoven anatase–rutile crystallites, where charge recombination is hindered by charge transfer and separation across phase interfaces [7–9]. Hydrogen peroxide is rapidly produced on its surface during AR1 photodegradation (Fig. 5), but it also undergoes rapid photocatalytic degradation by interaction with photogenerated species on the highly active photocatalyst surface (Fig. 7). The rate of H_2O_2 photocatalytic degradation soon overwhelms that of H_2O_2 formation, when the adsorption of organic species undergoing degradation starts to decline, and this would prevent higher H_2O_2 accumulation in the reaction system (Fig. 5). Completely different considerations (*vide infra*) should be taken into account when discussing the "anomalous" behavior of A9, evidenced in Fig. 6.

3.2.3. HCCOH photocatalytic degradation

Direct FA photolysis in aqueous solutions not containing the photocatalysts was excluded, as already verified under similar irradiation conditions [13]. In aqueous suspensions containing the TiO_2 particles, FA concentration always decreased at constant rate during irradiation, *i.e.* according to a zero-order rate law, in agreement with previous reports [13,30,31].

The photocatalytic activity scale of the investigated TiO_2 photocatalysts towards FA degradation can be appreciated in Fig. 8, reporting the zero-order rate constants of FA degradation determined in the presence of the investigated TiO_2 samples. The photoactivity scale is clearly different from that obtained in the photocatalytic degradation of the dye (Fig. 4). High surface area, pure anatase A284 and A136 proved to be the most active photocatalysts, even more efficient than P25. By contrast, low surface area pure anatase A9, which showed very active in AR1 photodegradation, exhibits extremely low photoactivity towards FA, even lower than that of pure rutile samples. Sol–gel and mixed phases home-synthesized TiO_2 samples showed all less active than mixed phase P25, and also of pure, high surface area anatase samples.

These results can be interpreted in the light of the different prevailing mechanisms at work in AR1 and FA photocatalytic degradation. In fact, azo dyes, as most organic molecules, usually undergo photodegradation through an oxidation path, initiated either by direct electron transfer to photoproduced h_{VB}^{+}, or by the attack of

hydroxyl radicals, formed upon h_{VB}^+-induced oxidation of water molecules or adsorbed –OH groups. Formic acid undergoes oxidative photodegradation to CO_2 mainly through direct interaction with conduction band holes, yielding the $CO_2^{\bullet-}$ radical anion, a highly reductant species [$E^\circ(CO_2/CO_2^{\bullet-}) = -1.8$ V]:

$$HCOO^- + h_{VB}^+ \rightarrow CO_2^{\bullet-} + H^+ \quad (3)$$

$CO_2^{\bullet-}$ can either originate the so-called current doubling effect [32] by injecting electrons into the semiconductor conduction band according to reaction (4), or rapidly react with O_2 yielding carbon dioxide [33], reaction (5):

$$CO_2^{\bullet-} \rightarrow CO_2 + e_{CB}^- \quad (4)$$

$$CO_2^{\bullet-} + O_2 \rightarrow CO_2 + O_2^{\bullet-} \quad (5)$$

The competitive reaction of FA with •OH radicals generated from water or hydroxyl anions oxidation is expected to be much slower [12,34]. In fact, the second order rate constants for aqueous phase •OH radical attack are $k = 1.3 \times 10^8$ M^{-1} s^{-1} for undissociated FA and $k = 3.2 \times 10^9$ M^{-1} s^{-1} for formate, whereas a higher value, $k = 1.7 \times 10^{10}$ M^{-1} s^{-1}, was reported for •OH radical attack on an azo dye similar to AR1 [35]. Furthermore, present FA photodegradation studies were carried out under natural pH conditions, comprised between the pK_a value of FA (3.75) and the point of zero charge of TiO_2 ($pH_{zpc} = 6.25$ [23]). This ensures maximum electrostatic attraction between FA, partly present as formate anion, and the positively charged TiO_2 surface.

High surface area TiO_2 samples, able to photocatalyse FA degradation through direct oxidation by h_{VB}^+, are thus very efficient (Fig. 8) and the surface area exposed to the water phase becomes the most important photocatalysts' structural feature in FA degradation. This accounts for the higher photoactivity of A136 and A284, particularly when compared to low surface area A9, A45 and R3, but also in comparison with the home-made sol–gel and mixed phase photocatalysts. Within these latter, the same relative activity scale is maintained in both AR1 and FA degradation (see Fig. 4 *vs*. Fig. 8); only ABR172 appears slightly more active in FA photodegradation, probably due to its high surface area. Rutile samples confirmed their limited photoactivity, practically independent of their surface areas.

A136 was more active than A284 in both AR1 and FA photocatalytic degradation, which might appear surprising in consideration of its lower surface area. However, the presence of amorphous layers has been evidenced on the surface of the A284 sample (see Fig. 8c of Ref. [18]), which may account for its lower photoactivity. The presence, content and effective role of amorphous parts of photocatalysts are difficult and complicated to prove [36].

3.2.4. H_2O_2 evolution during FA photocatalytic mineralization

No H_2O_2 could usually be detected in the aqueous phase during FA photodegradation in the presence of the investigated TiO_2 photocatalysts, its concentration remaining below 5×10^{-6} M. This confirms the results of previous studies of our [12,13] and other [37,38] research groups. Hydrogen peroxide does not accumulate during FA photocatalytic degradation on TiO_2 because it undergoes fast photodegradation on the photocatalyst surface.

In fact, the adsorption of substrates and intermediate species is expected to affect the interaction of H_2O_2 with the photocatalyst surface and consequently its photo-decomposition rate. When the photocatalyst surface is not significantly protected by adsorbed molecules, titanium peroxo complexes ($\equiv Ti^{IV}$–OOH) can form [39] and all electron transfer processes involving photogenerated species, able to oxidise or reduce the peroxo group, are consequently favored. Relatively good adsorption and high photocatalytic degradation rates of the substrate are thus pre-requisites for H_2O_2 accumulation under photocatalytic conditions. If the photocatalyst surface is not significantly protected by adsorbed molecules, as is the case of FA photodegradation occurring without the formation of any intermediate species, hydrogen peroxide undergoes faster decomposition on its surface. A ppm level of H_2O_2 was detected [40] only during the photocatalytic degradation of FA on TiO_2 thin films in an annular flow photocatalytic reactor. However, it quickly decomposed within the thin film surrounding the photocatalyst, so that its concentration was expected to hardly become high enough to be detected under batch reaction conditions [41].

However, most unexpectedly we detected hydrogen peroxide during FA photodegradation in the presence of A9. Its concentration slowly increased during the runs up to a maximum value, *ca*. 5×10^{-5} M, close to that attained during AR1 photodegradation on best performing P25 (Fig. 5), which was reached after 9000 s, when FA mineralization was almost complete, and then decreased.

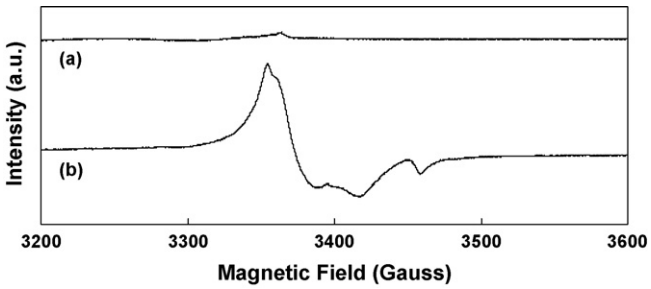

Fig. 9. EPR spectrum of (a) P25 and (b) sample A9.

3.3. Peculiarities of the A9 sample

The low surface area, pure anatase A9 sample thus exhibits a photocatalytic behavior very different from that of the other TiO_2 photocatalysts: it showed highly active in AR1 photocatalytic degradation, though this reaction apparently occurred in competition with H_2O_2 photoproduction, and it was rather inefficient in FA photomineralization, though being the only photocatalyst able to simultaneously evolve appreciable amounts of H_2O_2.

An explanation of this peculiar behavior was found when the EPR spectra of the investigated photocatalysts were recorded, at room temperature. Indeed, as shown in Fig. 9, the A9 sample gave a rather intense EPR signal, whereas the other photocatalysts were all EPR silent. This signal could be easily attributed to the presence of Ti^{3+} ions within A9, by comparison with the EPR spectra of reduced TiO_2 samples [42–44].

This can explain the higher reducing ability of this TiO_2 photocatalyst, testified by the much higher amount of H_2O_2 accumulated during FA degradation in the presence of this photocatalyst, and also provides a possible explanation of the quite peculiar behavior observed in AR1 photodegradation and parallel H_2O_2 photoproduction, *i.e*. quite fast AR1 photocatalytic degradation might occur through a reductive path in competition with H_2O_2 evolution. By contrast, A9 was a rather poor photocatalyst towards substrates which can only undergo oxidative degradation, such as FA in the present study, its lower efficiency possibly being related to the decrease of trapped holes observed in reduced TiO_2, due to deficiency of lattice oxygen trapping sites [42].

Reduced TiO_2 has been the subject of experimental and theoretical work [45]. The presence of Ti^{3+} ions is accompanied by the appearance of more than one EPR signal associated to various kinds of paramagnetic Ti^{3+} ions in the lattice and by the occurrence of a new state in the gap at about 0.8–0.9 eV below the conduction band, attributed to Ti^{3+} ions. Although the theoretical understanding of reduced TiO_2 is still unsatisfactory [46], it can be regarded as a very

interesting self-doped material, possibly able to absorb and display photoactivity under visible light [47,48].

4. Conclusions

The synergistic effect of mixed anatase and rutile phases typical of P25 confirms to be strictly related to its peculiar preparation method and structure. Besides on intrinsic features, such as crystalline phase composition, surface area, particles dimensions, surface hydrophilicity/hydrophobicity, the photocatalytic activity of TiO_2 photocatalysts and the prevailing photodegradation paths depend on the organic substrate to be degraded and possibly also on the presence of Ti^{3+} in the TiO_2 lattice.

Acknowledgements

The collaboration of Dr. Serena Cappelli in the EPR measurements and of Prof. Cesare Oliva in the assignment of the EPR spectrum is gratefully acknowledged. This research was financially supported by the University of Milan PUR funds, within the project *Photoinduced redox processes on semiconductor surfaces*.

References

[1] M.R. Hoffmann, S.T. Martin, W.Y. Choi, D.W. Bahnemann, Chem. Rev. 95 (1995) 69.
[2] A. Fujishima, T.N. Rao, D.A. Tryk, J. Photochem. Photobiol. C 1 (2000) 1.
[3] X. Chen, S.S. Mao, Chem. Rev. 107 (2007) 2891.
[4] A. Fujishima, X. Zhang, D.A. Tryk, Surf. Sci. Rep. 63 (2008) 515.
[5] J. Yu, J.C. Yu, M.K.-P. Leung, W. Ho, B. Cheng, X. Zhao, J. Zhao, J. Catal. 217 (2003) 69.
[6] T. Kawahara, Y. Konishi, H. Tada, N. Tohge, J. Nishii, S. Ito, Angew. Chem. Int. Ed. 41 (2002) 2811.
[7] D.C. Hurum, A.G. Agrios, K.A. Gray, T. Rajh, M.C. Thurnauer, J. Phys. Chem. B107 (2003) 4545.
[8] D.C. Hurum, K.A. Gray, T. Rajh, M.C. Thurnauer, J. Phys. Chem. B 109 (2005) 977.
[9] A. Di Paola, M. Bellardita, R. Ceccato, L. Palmisano, F. Parrino, J. Phys. Chem. C 113 (2009) 15166.
[10] J. Zhang, Q. Xu, Z. Feng, M. Li, C. Li, Angew. Chem. Int. Ed. 47 (2008) 1766.
[11] M. Mrowetz, E. Selli, J. Photochem. Photobiol. A 162 (2004) 89.
[12] M. Mrowetz, E. Selli, New J. Chem. 30 (2006) 108.
[13] M. Mrowetz, E. Selli, J. Photochem. Photobiol. A 180 (2006) 15.
[14] M. Mrowetz, E. Selli, Phys. Chem. Chem. Phys. 7 (2005) 1100.
[15] M. Mrowetz, A. Villa, L. Prati, E. Selli, Gold Bull. 40 (2007) 154.
[16] M.V. Dozzi, L. Prati, P. Canton, E. Selli, Phys. Chem. Chem. Phys. 11 (2009) 7171.
[17] G. Cappelletti, C.L. Bianchi, S. Ardizzone, Appl. Catal. B 78 (2008) 193.
[18] S. Ardizzone, C.L. Bianchi, G. Cappelletti, S. Gialanella, C. Pirola, V. Ragaini, J. Phys. Chem. C 111 (2007) 13222.
[19] A.C. Larson, R.B. Von Dreele, GSAS: General Structural Analysis System, Los Alamos National Laboratories, Los Alamos, NM, 1994.
[20] E. Selli, Phys. Chem. Chem. Phys. 4 (2002) 6123.
[21] C.G. Hatchard, C.A. Parker, Proc. R. Soc. London, Ser. A 235 (1956) 518.
[22] J.M. Joseph, H. Destaillats, H.M. Hung, M.R. Hoffmann, J. Phys. Chem. A 104 (2000) 301.
[23] C. Kormann, D.W. Bahnemann, M.R. Hoffmann, Environ. Sci. Technol. 125 (1991) 494.
[24] T. Shibata, H. Irie, M. Ohmori, A. Nakajima, T. Wanatabe, K. Hashimoto, Phys. Chem. Chem. Phys. 6 (2004) 1359.
[25] A.J. Hoffman, E.R. Carraway, M.R. Hoffmann, Environ. Sci. Technol. 28 (1994) 776.
[26] B. Jenny, P. Pichat, Langmuir 7 (1991) 947.
[27] X. Li, C. Chen, J. Zhao, Langmuir 17 (2001) 4118.
[28] T. Hirakawa, Y. Nosaka, Langmuir 18 (2002) 3247.
[29] G.T. Brown, J.R. Darwent, J. Chem. Soc., Faraday Trans. 1 80 (1984) 1631.
[30] G. Chester, M. Anderson, H. Read, S. Esplugas, J. Photochem. Photobiol. A 71 (1993) 291.
[31] N. Serpone, J. Martin, S. Horikoshi, H. Hidaka, J. Photochem. Photobiol. A 169 (2005) 235.
[32] E.R. Carraway, A.J. Hoffman, M.R. Hoffmann, Environ. Sci. Technol. 28 (1994) 786.
[33] J. Krýsa, G. Waldner, H. Měšťánková, J. Jirkovský, G. Grabner, Appl. Catal. B 64 (2006) 290.
[34] H. Park, W. Choi, J. Phys. Chem. B 108 (2004) 4086.
[35] G.V. Buxton, C.L. Greestock, W.P. Helman, A.B. Ross, J. Phys. Chem. Ref. Data 17 (1988) 513.
[36] B. Ohtani, Chem. Lett. 37 (2008) 217.
[37] C. Richard, P. Boule, J. Aubry, J. Photochem. Photobiol. A 60 (1991) 235.
[38] A.A. Ajmera, S.B. Sawant, V.G. Pangarkar, A.A.C.M. Beenackers, Chem. Eng. Technol. 25 (2001) 173.
[39] G. Munuera, A.R. Gonzalez-Elipe, J. Soria, J. Sanz, J. Chem. Soc., Faraday Trans. 76 (1980) 1535.
[40] F. Shiraishi, T. Nakasako, Z. Hua, J. Phys. Chem. B 107 (2003) 11072.
[41] F. Shiraishi, C. Kawanishi, J. Phys. Chem. B 108 (2004) 10491.
[42] T. Berger, M. Sterrer, O. Diwald, E. Knözinger, D. Panayotov, T.L. Thompson, J.T. Yates Jr., J. Phys. Chem. B 109 (2005) 6061.
[43] K. Komaguchi, H. Nakano, A. Araki, Y. Harima, Chem. Phys. Lett. 428 (2006) 338.
[44] F. Napoli, M. Chiesa, S. Livraghi, E. Giamello, S. Agnoli, G. Granozzi, G. Pacchioni, C. Di Valentin, Chem. Phys. Lett. 477 (2009) 135.
[45] V. Ganduglia-Pirovano, A. Hofman, J. Sauer, Surf. Sci. Rep. 62 (2007) 219.
[46] E. Finazzi, C. Di Valentin, G. Pacchioni, A. Selloni, J. Chem. Phys. 129 (2008) 154113.
[47] T. Ihara, M. Miyoshi, M. Ando, S. Sugihara, Y. Iriyama, J. Mater. Sci. 36 (2001) 4201.
[48] I. Justicia, P. Ordejón, G. Canto, J.L. Mozos, J. Fraxedas, G.A. Battiston, R. Gerbasi, A. Figueras, Adv. Mater. 14 (2002) 1399.